Structure and elastic properties of smectic liquid crystalline elastomer films

R. Stannarius,[1] R. Köhler,[1] U. Dietrich,[1] M. Lösche,[1] C. Tolksdorf,[2] and R. Zentel[2]
[1]*Institut für Experimentalphysik I, Universität Leipzig, Linnéstrasse 5, D-04103 Leipzig, Germany*
[2]*Institut für Organische Chemie, Universität Mainz, Duesbergweg 10-14, D-55099 Mainz, Germany*
(Received 30 November 2001; published 3 April 2002)

Mechanical measurements, x-ray investigations, and optical microscopy are employed to characterize the interplay of chemical composition, network topology, and elastic response of smectic liquid crystalline elastomers (LCEs) in various mesophases. Macroscopically ordered elastomer films of submicrometer thicknesses were prepared by cross linking freely suspended smectic polymer films. The cross-linked material preserves the mesomorphism and phase transitions of the precursor polymer. The elastic response of the smectic LCE is entropic, and the corresponding elastic moduli are of the order of MPa. In the tilted ferroelectric smectic-C^* phase, the network structure plays an important role. Due to the coupling of elastic network deformations to the orientation of the mesogenic groups in interlayer cross-linked materials (mesogenic cross-linker units), the stress-strain characteristics is found to differ qualitatively from that in the other phases.

DOI: 10.1103/PhysRevE.65.041707 PACS number(s): 61.30.Eb, 61.41.+e, 81.40.Jj, 61.10.Eq

I. INTRODUCTION

Liquid crystal elastomers (LCEs) have attracted much interest during recent years because of their unique combination of rubber elastic and anisotropic liquid crystalline properties [1–6] that open perspectives for novel, nondisplay applications. Of particular interest from a scientific point of view is the interplay of elastic, electric, and optical properties of the material. Macroscopic properties (form and strain) are coupled to the microscopic structure (order and orientation of mesogenic molecular segments, smectic layering).

Nematic elastomers have been extensively studied in the past. One of the most exciting features of these materials is their macroscopic form change as a result of the order-disorder transition of the mesogens. It has been proposed and successfully demonstrated [7,8] that this effect could form the basis of an artificial muscle. Compared to LC polymers, the LC elastomers possess a number of further advantages. A desired orientation of the samples can be achieved by mechanical stretching during the preparation [9,10]. Thus, LCEs promise to be interesting systems for the study of polymer backbone orientations (by mechanical fields) as well as mesogen orientation (by electrical fields) and various combinations. They are characterized by orientational order of the mesogenic groups as well as an anisotropy of the network. Unique interactions of electrical, optical, and mechanical properties have been reported (see, e.g. [11–16]).

In addition to the orientational order of the mesogens in the nematic phase, *smectic* elastomers exhibit a layered structure of the mesogenic units. Of particular interest are the smectic phases derived from polymers with chiral constituents [2]. In the smectic-C^* phase, the LC polymer can exhibit a spontaneous electric polarization. The elastomer network can stabilize a preferential orientation of the spontaneous polarization if the material is cross linked under appropriate conditions, but it is soft enough to allow ferroelectric reorientation of the mesogenic units. Weakly cross-linked elastomers provide form stability of the material while leaving the switching characteristics of the mesogens more or less intact. It is possible to influence mechanical and optical properties with external electric fields [17–21]. In addition, coupling of the orientation of the mesogenic units to the elastomer network leads to piezoelectric behavior. This has been first demonstrated with unoriented samples [22]. Ferroelectric, piezoelectric, and pyroelectric properties could be important for potential applications in sensor and actuator devices. Large electrostriction coefficients have been measured [23], and because of the comparably small elastic coefficients in the soft LCE material, one can achieve large deformations already at low electric fields, taking advantage of the electroclinic effect near the smectic-A to -C^* transition.

Structure, dynamics, and mechanical properties of ferroelectric LCE have been explored with various experimental methods such as dielectric spectroscopy [24], Fourier transform infrared [25,26], atomic force microscopy [27], interferometry [23,28,29], nonlinear optics [30], and mechanical methods [31–37]. However, some fundamental structural properties are still only poorly understood, and many of the possible electro-opto-mechanical interactions predicted theoretically have not been analyzed experimentally so far.

The goal of this study is the structural assessment of ordered (''single crystal'') smectic LCE films and a quantitative measurement of their mechanical properties. The particular choice of the material was motivated by studies of electromechanical and related effects of similar substances (e.g., [23–29]).

First, we explore the molecular structure of substrate supported and freely suspended films of smectic elastomers. We discuss the influence of cross linking on the smectic layer structure and the dependence of temperature, mesophases, and external stress on the films. The influence of order-disorder transitions of the mesogenic units on the macroscopic shape of smectic LCE is investigated. Viscous and elastic properties of the materials are measured by exposing smectic LCE balloons [32] to mechanical stress. A pressure-radius relation is established in the different mesophases and data are interpreted within elasticity models. We discuss the relations between elastic behavior, network topology, and mesogenic ordering.

TABLE I. Structure, cross-linker content x, and mesomorphism of the investigated materials.

Sample	Structure	x	Phase sequence
Inter3/05	Fig. 1(a)	0.05	Sm-*X*, 65 °C; Sm-*C**, 95–96 °C; Sm-*A*, 125 °C Iso.
Inter3/25	Fig. 1(a)	0.25	Sm-*X*, 52 °C; Sm-*C**, 89–90 °C; Sm-*A*, 132 °C Iso.
Intra2/25	Fig. 1(b)	0.25	Sm-*X*, 24 °C; Sm-*C**, 46–48 °C; Sm-*A*, 67–69 °C Iso.

II. EXPERIMENT

A. Samples

The synthesis of the precursor polymers used in this study has been described in detail [32]. The random side-chain copolymers consist of a siloxane backbone with attached mesogenic groups and cross-linker units. The substituents are statistically distributed on the siloxane chain. The ratio of nonsubstituted, mesogen substituted, and cross-linker substituted backbone units is $2.7:(1\text{-}x):x$, where cross-linker fractions x are between 0.05 and 0.25. The structure of the cross-linker unit has significant influence on the formation of the elastomer network. It has been demonstrated that the siloxane backbone and the mesogenic substituents in the smectic mesophases are segregated and the backbone is essentially sandwiched between adjacent mesogen layers [38]. If the length of the cross-linker unit is comparable to that of the mesogens, a three-dimensional network can be formed. For this network topology, the term *interlayer* cross-linked elastomer has been coined. In contrast, if the cross-linking substituent is much shorter than the mesogens, it cannot establish connections between backbone segments in adjacent siloxane layers. Then, interconnections of the network normal to the smectic layers are predominantly mediated by the main chains crossing the mesogenic layers. In that case, the network will be more or less two dimensional. This situation will be referred to as *intralayer* topology. The notations, structures, and phase sequences of the un-cross-linked polymers are given in Table I.

The relative amount of cross-linker groups provides only a qualitative measure of the cross-linking density of the network after UV irradiation. Within a set of materials that differ only in the relative amount of cross-linker substituents, the cross-linking density will increase with the volume fraction of photoreactive groups. When materials with different network topologies are compared, there is no direct relation between the relative amount of photoreactive groups and network density since the functionalities of the groups at different substituents may differ.

B. Sample preparation

Elastomer balloons of a spherical geometry were obtained by UV cross linking of smectic bubbles (spherically deformed polymer films), prepared by a technique described earlier [32,39]. In this procedure, freely suspended films are drawn on the open end of vertical glass capillaries (1.0 mm inner diameter, ≈ 2.5 mm outer diameter). The capillary end is roughened to improve the contact of the elastomer to the glass surface after cross linking. The film is inflated into smectic bubbles by slowly blowing a controlled volume of air into the capillary using a microliter syringe. The polymer bubbles are very sensitive to rupture while they are drawn or inflated. The optimum temperature to produce the bubbles is about 10–25 K above the smectic-to-isotropic bulk transition where the viscosity is considerably lower than in the smectic phases. It turns out that bubbles inflated in the isotropic phase are robust and persist for hours, sufficiently long to perform optical investigations. Most probably, surface induced ordered layers stabilize the film against thickness fluctuations to a certain extent. The bubbles are subsequently cooled into the smectic-*A* (Sm-*A*) phase. A uniform sample orientation forms due to the layer ordering parallel to the film surface in the freely suspended smectic films.

The balloons are photo-cross-linked by illumination with diffuse UV light [32] in the Sm-*A* phase. The direct beam on the bubble is blocked. This is necessary to avoid an inhomogeneous formation of the elastomer network, which may lead to the rupture of the bubbles during cross linking. Since the UV intensity is reduced by the indirect illumination method, we choose illumination times of 1 h. This is sufficient to drive the cross-linking reaction to completion even with the low UV intensity. Already after 30-min illumination, the elastic properties of the films remain constant.

C. Experimental setup

All experiments were performed in a temperature controlled copper box with glass observation windows and a UV illumination window. For the x-ray experiments, the glass observation windows were replaced by Kapton films. Figure 2 sketches the setup schematically. The temperature in the box was stabilized with an accuracy better than 0.5 K and measured with a sensor located in the air near the film. A quartz window for UV illumination is at the top of the box, a beam stopper blocks the direct UV beam, and the inner walls of the box have been wrapped with aluminum foil to achieve multiple reflections of the UV beam in the box, providing a uniform bubble illumination. For optical observation (long-range microscopy, determination of film thickness, and radius measurements) the bubbles/balloons [40] were illuminated with monochromatic, unpolarized parallel light. Transmission images were recorded with a charge-coupled device camera and digitally processed. The relative radii changes of elastomer balloons have been determined by comparing the images of the mechanically expanded balloon with the digitally resized and shifted image of the original (stress-free) balloon. The stretching factor yields the ratio of stretched and original radii. Since the center of the expanded balloon sphere shifts relative to the capillary, the digital shift parameters as well as the comparison of the image shapes

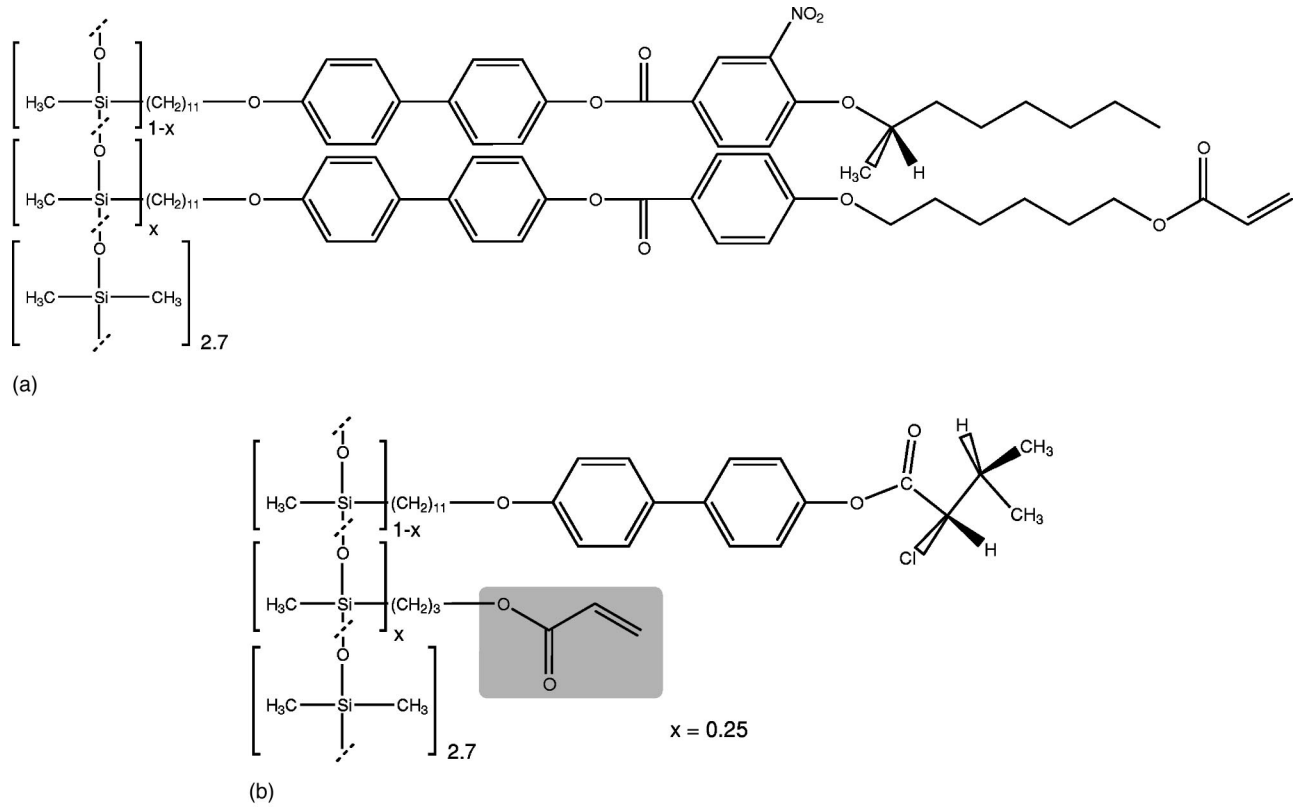

FIG. 1. Chemical composition of the precursor copolymers. (a) Interlayer three-kernel materials Inter3/25 with $x=0.25$, Inter3/05 with $x=0.05$, and (b) intralayer two-kernel material Intra2/25 with $x=0.25$.

provide a test for the uniform expansion of the elastomer balloons. With the particular materials studied here, elasticity measurements in balloon geometry are preferable over the alternative approach of uniaxial stretching of planar films. The preparation of the thin planar films, in particular cutting the elastomer films from their lateral supports after cross linking, poses much more technical problems than the bubble preparation.

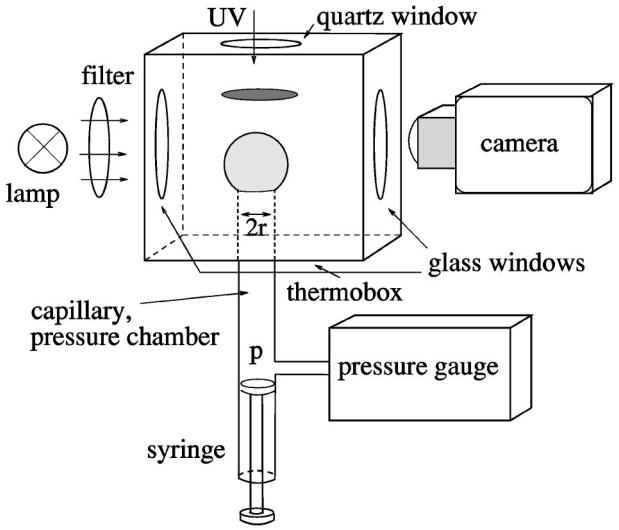

FIG. 2. Schema of the experimental setup for sample preparation and mechanical measurements.

Small-angle x-ray diffraction (SAXD) for smectic balloons was performed in an x-ray spectrometer of local design [41] in which the incoming and the scattered beams lie in a vertical plane. The x-ray source (AXS Bruker) is a sealed Cu tube whose white beam feeds a graded parabolic W/Si mirror (''Goebel mirror'') transmitting the Cu-K_α line ($\lambda = 0.1542$ nm). The impinging beam is conditioned by a pair of horizontal entrance slits, confining it to ≈ 80 μm in the vertical direction. It is directed towards the top of the spherical balloon where the smectic layers, with a thickness of the order of 5 nm, give rise to Bragg scattering at an angle 2θ ($\approx 1.8°$), cf. Fig. 4. The scattered beam is received in a vertically oriented position-sensitive detector (M. Braun, Garching). A diffuse background stemming from the Kapton windows of the container has been subtracted from the raw data.

For optical characterization, we have used an Axiotech reflected light polarization microscope (Carl-Zeiss Jena), and a QM 100 long-range microscope (Questar).

III. RESULTS

A. Optics

A first examination of the material was performed by means of optical reflection microscopy. The transition from the Sm-*A* phase to the isotropic phase has been established for all samples before and after cross linking by means of birefringence measurements. In the native material, Sm-*A* focal conic textures are observed in thin cells with untreated

glass plates. At the transition to the isotropic phase, the birefringence vanishes within a temperature interval of about 2 K. After cross linking, the texture in the Sm-*A* phase persists. The phase transition to the isotropic state in the elastomer is also characterized by an almost complete disappearance of the optical birefringence. The transition is more heterogeneous than in the native sample and the transition interval is slightly broadened. In the isotropic phase, a faint, structured birefringence pattern remains. We attribute this to a weak anisotropy of the polymer network. It is, however, clearly smaller, by at least one order of magnitude, than the birefringence in the Sm-*A* mesophase.

The film thickness, which is essential for the determination of elastic moduli, is determined in the isotropic phase from the optical transmission images by means of reflectometry [42]. In most cases, the polymer bubbles are not uniform in their film thickness. Typically, a film thickness gradient is found from top to bottom, which is stable during observation times of a few hours. In addition, the film thickness can vary locally by about 10%. The number of smectic layers is not uniform in the film even after long annealing times. When the polymer bubbles are cooled into the Sm-*A* phase, they become turbid. Structural rearrangements take place in the films during the transition to the ordered phase. Their nature is best investigated by means of reflection microscopy of planar films.

Figure 3 shows reflection images of a planar free-standing film with highly inhomogeneous thickness, taken in unpolarized white light during cooling from the isotropic to the Sm-*A* phase. In the isotropic phase, the film thickness varies continuously in the film plane. At the phase transition [Fig. 3(a)] randomly distributed ''islands'' are nucleated. After annealing in the Sm-*A* phase for about 1/2 h before UV irradiation, these islands gradually disappear [Fig. 3(b)]. The thickness steps seen in this image correspond to individual ordered smectic layers. The process is reversible. When the polymer film is reheated into the isotropic phase, the layer steps disappear and the film thickness variation becomes continuous again. This indicates that a rearrangement of the macroscopically disordered polymer to an ordered smectic takes place at the phase transition, and that the layers are perfectly stacked in the film plane. After cross linking in Sm-*A*, the thickness steps remain permanent in all phases. In color images of inhomogeneous Sm-*A* Inter3/05 films at 120 °C, approximately 10–12 color steps are counted between second-order blue regions (film thickness of about 210 nm) and second-order yellow regions (film thickness of about 270 nm). The single step size of 5 ± 1 nm is in good agreement with the x-ray data (see the following section) of smectic layer spacing.

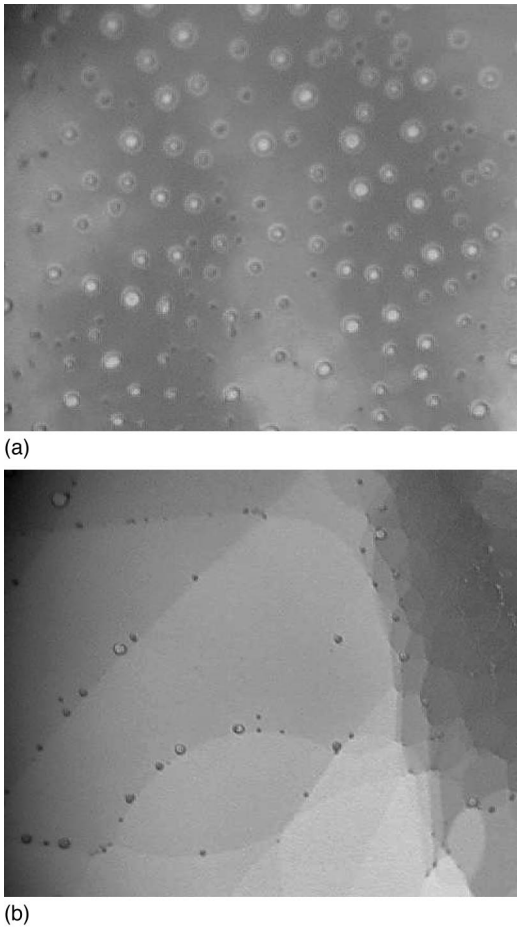

FIG. 3. Images of a freely suspended polysiloxane film of Inter3/05 in the isotropic phase at the transition to Sm-*A*, 124 °C (a) and in the smectic-*A* phase at 120 °C (b). Both the images show a 240 μm$\times$200 μm top view of the film in white, unpolarized light.

B. X-ray diffraction

In an earlier investigation [34], we have measured the room temperature x-ray reflectivity of a spin coated Inter3/05 film on a silicon wafer before and after cross linking in the Sm-*A* phase. The data indicated a long-range periodic order, with smectic layers parallel to the substrate. The layer structure and orientation were found to be preserved during cross linking. A shift of the peaks to larger angles by about 1% indicated a slight influence of cross linking on the smectic LCE layer spacing.

Temperature dependent small-angle x-ray diffraction measurements have been performed on elastomer balloons in the geometry as shown in Fig. 4. In this geometry, x-ray diffraction data can be obtained from free-standing films without contributions from the meniscus material. The beam height ($\approx$80 μm) is much larger than the film thickness ($\approx$1 μm) but significantly smaller than the balloon diameter ($\approx$3 mm). Because of the large balloon radii compared to the smectic layer thickness, the layers may be considered planar on a molecular level.

Figure 5 shows diffraction measurements of Inter3/05 during the transition from the Sm-*A* phase to the isotropic phase. The peak evidences a parallel alignment of smectic layers in the film plane. It vanishes gradually within a temperature interval of about 5 K. The transition is observed around the same temperature as in bulk samples of the precursor polymer. The smectic layer reflex is completely absent in the isotropic phase of the cross-linked material, i.e., smectic layer order and orientational order of the mesogenic units

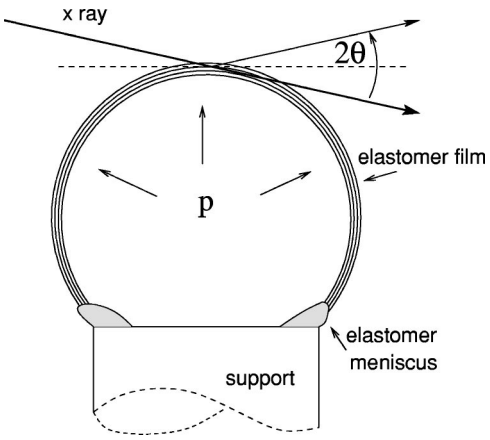

FIG. 4. Schematic view of the geometry of the small-angle x-ray diffraction experiment. The balloon diameter is of the order of 3 mm, the film thickness is in the submicrometer or micrometer range. The x-ray beam has a height of 80 μm. For clarity, the scattering angle 2θ has been greatly exaggerated.

(indicated by the optical birefringence observations, cf. preceding section) vanish concurrently, as in the native polymer. Obviously, the optically observed thickness steps indicate only the surface structure of the films whereas the internal layer structure melts upon entering the isotropic state. When the sample is cooled down to the Sm-*A* phase again, the smectic layer structure reappears. The same behavior is qualitatively observed in Intra2/25, the (intralayer) elastomer derived from the precursor copolymer with 25% cross-linker density.

Figure 6 shows the temperature dependence of the layer spacing for the two samples, Inter3/05 and Intra2/25. The

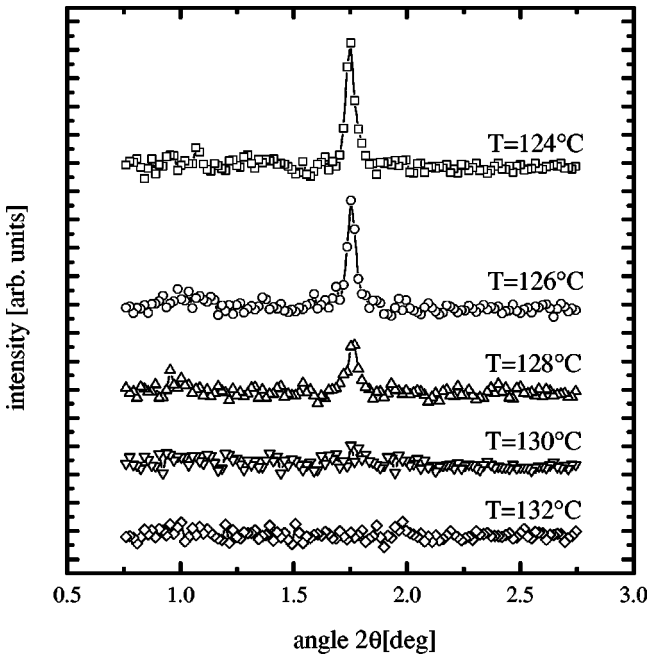

FIG. 5. Temperature dependence of the first-order SAXD peak originating from the smectic layer in an LCE balloon of Inter3/05 at the Sm-*A* isotropic transition.

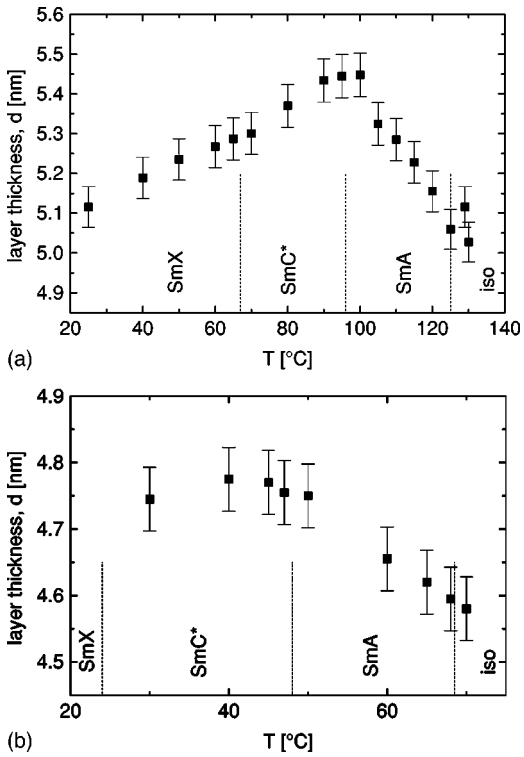

FIG. 6. Temperature dependence of the smectic layer spacing in Inter3/05 (a) and Intra2/25 (b). The spacings have been derived from x-ray spectra such as those shown in Fig. 5 under the assumption that the peak around $2\theta = 1.75°$ corresponds to the first-order Bragg diffraction of the stratified film, i.e., $d = \lambda/[2\sin(2\theta/2)]$. The bulk phase transition temperatures of the native polymers are indicated by dashed lines.

smectic layer thickness increases when the sample is heated within the Sm-*C** phase. This can be explained with the assumption of a temperature dependent tilt angle within the Sm-*C** phase. From room temperature (25 °C) to the Sm-*C**/Sm-*A* transition ($T \approx 95$ °C) in Inter3/05, the layer thickness *d* grows by about 6%. No discontinuities are found at the smectic mesophase transitions. A tilt angle variation from $\approx 20°$ at room temperature to zero at the Sm-*C**/Sm-*A* transition is consistent with the observed layer thickness changes. This is in good quantitative agreement with measurements of ferroelectric switching angles [21]. In comparison, the contribution of thermal expansion of the material to size changes is lower by one order of magnitude.

The smectic layer thickness decreases with increasing temperature in the Sm-*A* phase ($\Delta d/d \approx -2 \times 10^{-3}$ per Kelvin of ΔT for Inter3/05). Among the effects that could be responsible for such a remarkable layer shrinkage are the temperature dependence of the order parameter of the mesogens and/or a temperature dependent interdigitation of the smectic layers. The effect is qualitatively similar for the samples with different network topologies and cross-linker densities. Therefore, we assume that its origin is primarily related to the mesogen properties rather than to the network structure. Qualitatively similar behavior has been observed in the native polymers [43] in x-ray measurements of substrate-supported films.

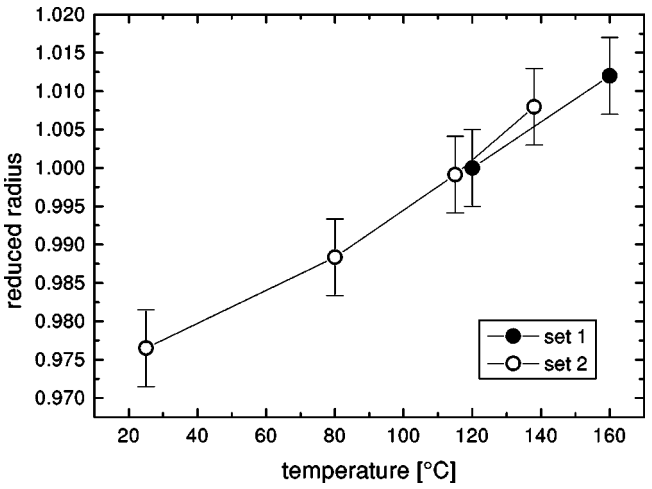

FIG. 7. Temperature dependence of the relaxed radius of an Inter3/05 balloon.

C. Thermomechanical characterization

Some nematic LC elastomers possess the unique property to respond with macroscopic shape distortions on the change of orientational order of the mesogenic units [8]. The effect reaches remarkable amplitudes in the vicinity of an order-disorder transition. In the Sm-*A* to isotropic transition of the smectogens studied here, it is natural to expect similar effects near the clearing temperature if the backbone chain conformation is coupled to the mesogenic orientation. Radii of stress-free balloons of Inter3/05 are shown in Fig. 7 as a function of temperature. The balloon radii have been determined at a very low, inner excess pressure p of about 10 Pa (necessary to maintain the spherical shape of the balloons). They have been normalized to the radius measured at 120 °C. The very small remaining strain can be corrected on the basis of the stress-strain curves (see below) by extrapolation to $p=0$. However, this correction changes the results by less than 0.5% and is practically insignificant.

The graphs indicate a continuous increase of the balloon radii with temperature regardless of the phase state. In particular, no anomalies are observed in the vicinity of the phase transition temperatures. The data are consistent with a linear expansion of the elastomer film. The linear expansion coefficient $\alpha=2.8\times10^{-4}$ K^{-1} determined from the data in Fig. 7 is in agreement with typical volume expansion coefficients $\gamma=3\alpha$ for organic liquids, in particular for low molecular mass nematic mesogens. The same behavior has been qualitatively observed for the Intra2/25 and Inter3/25 materials.

D. Elasticity measurements

When the internal pressure in an elastomer balloon is changed, the radius adopts a new equilibrium between excess pressure and elastic forces within the film. The elastic forces consist of a static and a dynamic (Maxwell) contribution. If the strain is low ($<5\%$), the response of the balloon radius to a pressure change is instantaneous within the temporal resolution of the measurement, and the deformation is completely reversible. For larger strain, however, slow dynamic effects and irreversible deformations can occur.

Figure 8 shows experimental, static stress-strain curves for Inter3/05 in different mesophases. We started with a stress-free balloon at a given temperature and increased the inner excess pressure successively (in steps of approximately 10 Pa) by pumping small amounts of air into the balloon. After a maximum expansion that reached up to 30% in the Sm-*C** and Sm-*A* phases, the balloon was deflated again. Time intervals of about 30 s between successive pressure steps were sufficient for the establishment of the stationary equilibrium deformations, except in the low-temperature measurements where pronounced hysteresis loops were observed. These are due to a very slow relaxation component (time constant >60 s near room temperature). In some cases, a permanent deformation remained after the inflation/deflation cycle of ''virgin'' balloons. In the experiment presented in Fig. 8, the deformations were completely reversible. The initial stress-free balloon radius was $R_0=2.71$ mm and the film thickness varied from 0.85 μm at the top to 1.0 μm at the bottom. A qualitative comparison of the stress-strain characteristics shows that the difference between the elastic characteristics in the isotropic and Sm-*A* phases is marginal: The mesogenic order has no measurable influence on the mechanical properties. Only in the tilted Sm-*C** phase, a qualitative change was observed. An interpretation of the characteristic nonlinear shapes of the expansion curves requires suitable elasticity models that are introduced in the following section. We note that comparison of the curves measured by using one individual balloon at different temperatures yields valuable and precise information on the differences in the individual mesophases, and the curves can be directly compared without any knowledge of the film thickness. For comparison of data obtained from different balloons and a quantitative determination of the elastic moduli, knowledge of the film thickness is, however, essential. In fact, uncertainties in this thickness represent the largest error source in the determination of absolute values of elastic moduli.

In Fig. 9, typical experimental results for the intralayer elastomer Intra2/25 are presented. Qualitative differences of the elastic properties in the Sm-*A* and Sm-*C** phases are not observed. However, the hysteresis is much more pronounced in Sm-*C** because of the lower temperatures [45]. The film thickness in this balloon was not uniform enough to allow a calculation of the absolute value of the elastic modulus. In previous measurements, the modulus of Intra2/25 was determined to be of the order of 3 MPa [32]. It was found to increase slightly with temperature in the Sm-*C**, Sm-*A*, and isotropic phases.

IV. DISCUSSION

A. Elasticity models

The equations describing the inflation of a uniform elastomer balloon under the action of an excess internal pressure can be established from an evaluation of the elastic energy associated with its expansion. The radius changes dR of the elastomer balloon in response to an internal excess pressure p is obtained by equating the elastic energy to the work, $p\times4\pi R^2dR$, done by the gas inside the balloon.

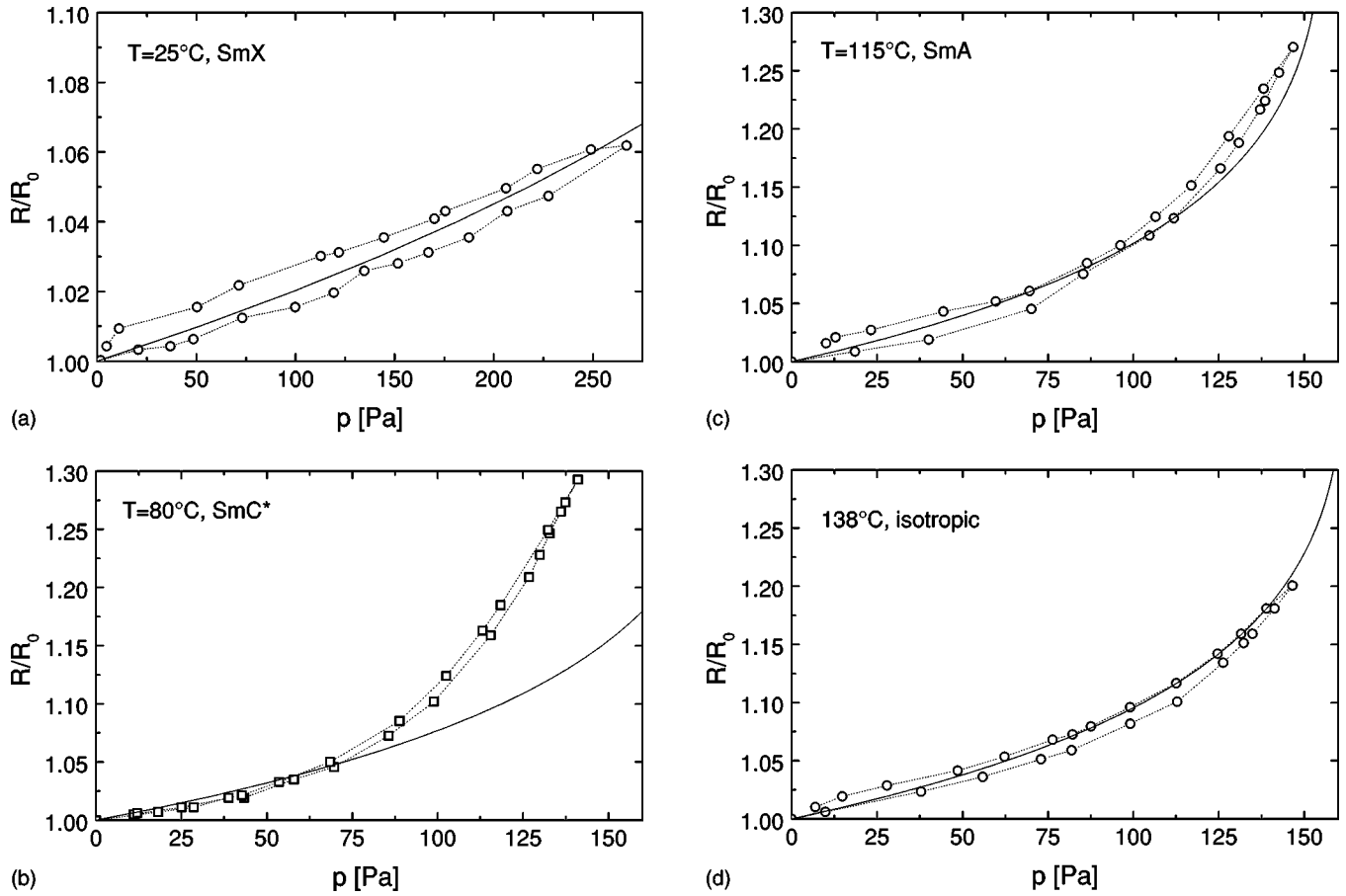

FIG. 8. Pressure-radius relation in Inter3/05 balloons at temperatures of 25 °C in Sm-*X* (a), 80 °C in Sm-*C** (b), 115 °C in Sm-*A* (c), and 138 °C in the isotropic phase (d). The solid curves indicate the behavior expected according to the Mooney-Rivlin model and $C_2=0$ with fit parameters $\tilde{C}_1=850$ Pa (a), $\tilde{C}_1=280$ Pa (b), $\tilde{C}_1=250$ Pa (c), and $\tilde{C}_1=260$ Pa (d).

A suitable elasticity model has to be chosen. Conventional linear elastic theories have been developed for isotropic as well as anisotropic rubbers. These theories assume infinitesimally small deformations of the material and establish a linear relation between the stress and strain tensors. The coefficients in such a relation represent the elastic moduli of the material.

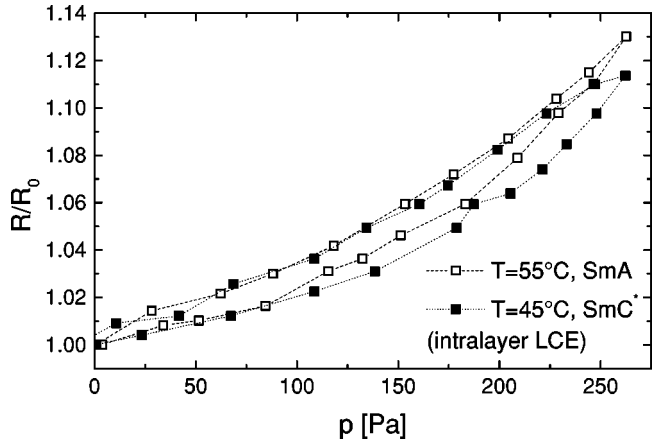

FIG. 9. Pressure-radius relation in Intra2/25 balloons at temperatures 45 °C in Sm-*C** (■), and 55 °C in Sm-*A* (□). Solid curves indicate the behavior expected according to the Mooney-Rivlin model and $C_2=0$ with fit parameters $\tilde{C}_1=550$ Pa (■) and $\tilde{C}_1=580$ Pa (□).

Naturally, these models are restricted to a linear description of the stress-strain curves in the elastomer balloons, which is only valid in the limit of small strain. Since the deformations observed in the experiments are pronouncedly nonlinear (cf. Figs. 8 and 9), we will instead use the phenomenological Mooney-Rivlin model (see, e.g. [44]) to obtain the relation between the elastic free energy density f_{el} and the balloon expansion. This model has been developed for *isotropic* rubbers. It establishes a relation between the three invariants I_1, I_2, I_3 of the Cauchy strain tensor λ_{ij} and the scalar free energy expression [44] but does not explicitly assume infinitesimally small deformations. The invariants

$$I_1=\lambda_{xx}^2+\lambda_{yy}^2+\lambda_{zz}^2-3,$$

$$I_2=\lambda_{xx}^2\lambda_{yy}^2+\lambda_{yy}^2\lambda_{zz}^2+\lambda_{zz}^2\lambda_{xx}^2-3,$$

$$I_3=\lambda_{xx}^2\lambda_{yy}^2\lambda_{zz}^2-1,$$

are connected with three material coefficients C_1, C_2, C_3 to yield $f_{el}=C_1I_1+C_2I_2+C_3I_3$.

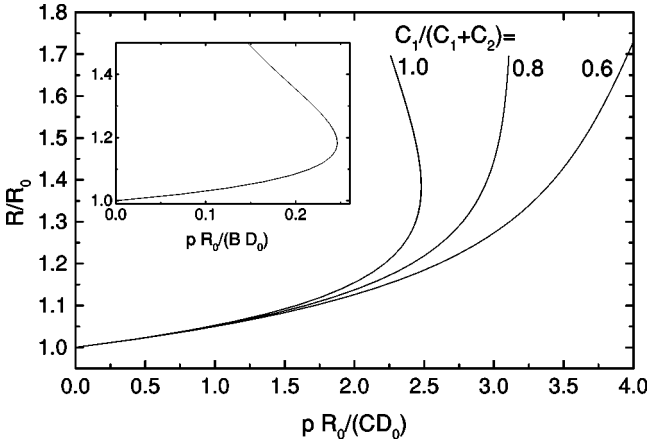

FIG. 10. Pressure-radius characteristics according to the Mooney-Rivlin model, Eq. (1), for constant $C=C_1+C_2$ and different ratios of C_1/C as indicated. Inset: Pressure-radius characteristics according to the smectic layer compression model [Eq. (4)].

The first coefficient, $C_1=N^*kT/2$, comprises a free energy expression for an ideal network, with N^* being the number of elastically active chains per unit volume. The coefficient C_3 is connected with volume changes of the material (i.e., its bulk modulus). It is much larger than the other two coefficients. Therefore, one may use the incompressibility condition, $\lambda_{xx}\lambda_{yy}\lambda_{zz}=1$. The model yields [32]

$$p=\frac{4D_0}{R_0}\left[C_1\left(\frac{R_0}{R}-\frac{R_0^7}{R^7}\right)+C_2\left(\frac{R}{R_0}-\frac{R_0^5}{R^5}\right)\right], \tag{1}$$

where R_0 is the relaxed radius and $D_0 \ll R_0$ is the thickness of the relaxed film. For small deformations, $\varepsilon=(R-R_0)/R_0 \ll 1$, the equation can be expanded in ε, and only the sum of both coefficients $C=C_1+C_2$ enters the linearized relation

$$p=6C\frac{4D_0}{R_0}\varepsilon. \tag{2}$$

In previous investigations, the LCE materials Inter3/25 and Intra2/25 with high cross-linker densities have been characterized [32,33]. Since the expansions did not exceed 5%, the stress-strain curves are allowed to fit only the linear coefficient C.

The nonlinear characteristics of Eq. (1) is of course specific for the underlying model. For the ideal case $C_2=0$, there exists a pressure extremum at $R\approx 1.383R_0$. Figure 10 shows the pressure versus radius curves for different values of C_1 and C_2, where the sum C_1+C_2 has been kept constant and the coefficients themselves are considered independent of strain.

An alternate ansatz to describe elasticity is the linearized stress-strain relation $\sigma_{ij}=c_{ijkl}\varepsilon_{kl}$, which may account for nonisotropic elastic properties of the material [5,46]. For the uniaxial case (symmetry axis z), the nonvanishing coefficients are [46]

$$c_{xxxx}=c_{yyyy}=\lambda+2G,$$

$$c_{zzzz}=\lambda+2G+\beta,$$

$$c_{xxyy}=c_{yyxx}=\lambda+2\rho,$$

$$c_{xxzz}=c_{yyzz}=\lambda+\delta,$$

$$c_{xyxy}=G-\rho,$$

$$c_{xzxz}=c_{yzyz}=G.$$

The linearized pressure-radius relation in this model yields [47]

$$p=[3G+\beta+\rho-2\delta]\frac{4D_0}{R_0}\varepsilon. \tag{3}$$

For an isotropic rubber, all coefficients except G vanish and one obtains a relation analogous to Eq. (2). Of course, this linear model is not suitable to describe more than the initial slope of the $p(R)$ characteristics in the small-strain limit. The Hook modulus of an isotropic rubber is related to the coefficients introduced above by $E=3G=6C$.

So far, the smectic layer structure has not been accounted for in the models. In the smectic phases, another contribution to the elasticity of the balloons may arise from the contraction of the film normal to its plane. As the local in-plane isotropic stress causes the membrane to stretch uniformly in all directions in the layer plane, the elastomer is forced to contract normal to the layers as a consequence of its incompressibility. If one assumes that the film thickness change is entirely achieved by a compression of the individual smectic layers, the layer compression modulus B enters the free energy expression as [48]

$$f_{sm}=\frac{1}{2}B\left(\frac{du}{dz}\right)^2,$$

where u is the smectic layer displacement. This leads to an additional contribution to the $p(R)$ curve [32]

$$p=2\frac{D_0}{R_0}B\left(\frac{R_0^5}{R^5}-\frac{R_0^7}{R^7}\right)\approx B\frac{4D_0}{R_0}\varepsilon. \tag{4}$$

The graph of this equation is shown in the inset of Fig. 10. Since the x-ray results indicate a complete melting of the layer structure into the isotropic phase on heating, the layer compression modulus should be effective only in the smectic state. The experimental fact that the quantitative changes of the stress-strain curves near the clearing point are marginal leads to the conclusion that the influence of the smectic layer compression is probably much smaller than that of the entropic elasticity contributions.

B. Application to the experimental results

Before the model calculations are applied to interpret the experimental data as shown in Figs. 8 and 9, two remarks are necessary. First, the balloons are not complete spheres since

they are supported on a capillary. However, one can easily verify from the mapping of inhomogeneities or particles on the balloon surface that the strain is uniform on the film plane such that the equations can be applied to describe the pressure-radius relations of the incomplete sphere adequately. The performance of the optical imaging and image processing (see above) is sufficient to detect any deviations of the balloon shape from its shape at zero stress. Hence deformations that lead to nonuniform expansion can be excluded from the data analysis. Second, the film thickness of the balloons is not completely uniform. In the balloon characterized in Fig. 8, it increased by more than 15% from top to bottom, and even locally the film thickness varied slightly. This is insignificant when we discuss the stress-strain curves of an individual balloon at different temperatures, but it leads to an absolute uncertainty of 25% of the elastic parameters.

Since the film thickness D_0 is the largest source of error in the determination of the absolute values of elastic moduli, we introduce the specific moduli $\tilde{C}_i=(4D_0/R_0)C_i$, which can be directly compared for all stress-strain curves of an individual sample in various phases, such as the Inter3/05 balloon in Fig. 8. The dotted lines in Figs. 8(a)–8(d) represent fits to Eq. (1), where an ideal rubber behavior has been assumed ($C_2=0$). In the isotropic phase [Fig. 8(d)], the hysteresis of the inflation-deflation curves is negligibly small. The curve can be fitted satisfactorily with the Mooney-Rivlin model by setting $\tilde{C}=\tilde{C}_1+\tilde{C}_2=260$ Pa. Within experimental accuracy, any value of C_2 in the range $0<C_2/C_1<0.1$ is consistent with the measured data as long as $\tilde{C}$ is kept constant. In the Sm-*A* phase [Fig. 8(c)], the $p(R)$ curve is qualitatively unchanged from that observed in the isotropic phase. The fit gives $\tilde{C}=250$ Pa. In the Sm-*C** phase [Fig. 8(b)], the low-strain data ($R/R_0<1.05$) can be fitted with $\tilde{C}=300$ Pa. However, it is not possible to fit the complete characteristics with any parameter set (C_1,C_2) within the Mooney-Rivlin model. This indicates that another mechanism dominates the elastic behavior in the Sm-*C** phase. A possible explanation is the coupling of the elastic deformations to the mesogenic tilt, which is discussed in more detail in the following section. In the low-temperature Sm-*X* state [Fig. 8(c)], the hysteresis is quite large and the strain achieved at comparable stresses is much lower than in the other phases. A fit yields a larger modulus, $\tilde{C}=900$ Pa.

With the geometric characteristics of the balloon (radius $R_0=2.71$ mm and the average film thickness $D_0\approx0.9$ μm), the elastic modulus $E=6C$ of Inter3/05 is $E\approx1.24$ MPa (isotropic, 138 °C), $E\approx1.19$ MPa (Sm-*A*, 115 °C), $E\approx1.4$ MPa (Sm-*C**, 80 °C, $R/R_0<1.05$), $E\approx4.3$ MPa (Sm-*X*, 25 °C). The relative uncertainties are smaller than 10%. Compared to Inter3/25, the structurally equivalent material with 25% cross-linker groups, the elastic modulus is somewhat smaller but of the same order of magnitude [32]. We note that the accuracy of the present experiment is much higher than that of the Inter3/25 measurements where only $\approx5\%$ strain was achieved.

For the Intra2/25 elastomer, the Mooney-Rivlin model fits the experimental data, shown in two exemplary measurements in Fig. 9, in all phases satisfactorily. In contrast to the interlayer Inter3/05 balloon, no qualitative differences distinguish the Sm-*C** phase from the high-temperature phases. The moduli determined at different temperatures are $\tilde{C}=660$ Pa (isotropic, 85 °C), $\tilde{C}=600$ Pa (isotropic, 75 °C), $\tilde{C}=550$ Pa (Sm-*A*, 65 °C), $\tilde{C}=560$ Pa (Sm-*A*, 55 °C), $\tilde{C}=580$ Pa (Sm-*C**, 45 °C), and $\tilde{C}=690$ Pa (Sm-*C**, 35 °C). Their variation is within the relative experimental uncertainty of 10%.

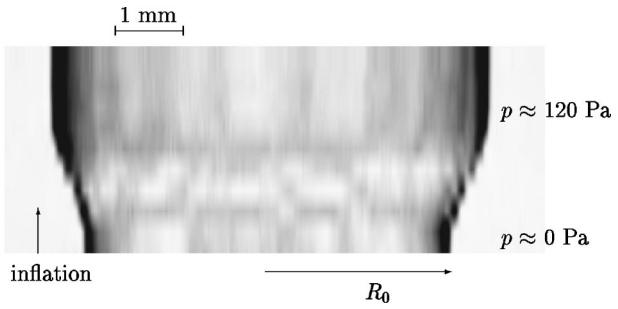

FIG. 11. Equatorial cross section of an Inter3/05 balloon (initial film thickness $D_0\approx1$ μm) in yellow monochromatic light (0.589 μm). As the film thickness decreases with increasing lateral strain of the balloon, the interference order changes in agreement with the thickness contraction factor of ≈0.7 as estimated from volume conservation (see text).

As a consequence of the volume conservation of the elastomer, a film thickness variation proportional to the inverse square of the radius change is expected. This can be confirmed, although with relatively poor accuracy, from the optical inspection of the balloons in transmitted monochromatic light. As a typical example, we present images of an Inter3/05 balloon at 80 °C. Figure 11 shows a stack of equatorial cross sections in yellow monochromatic light ($\lambda=589$ nm), with the time t as the vertical coordinate. In the course of the experiment, the internal excess pressure has been increased from zero to 120 Pa, and the graph visualizes the continuous transition of the balloon diameter and relative film thickness in response to the pressure change. The horizontal intensity variations of the transmitted light indicate that the film thickness of this balloon is not completely uniform. Between different equatorial positions, the order of interference varies slightly. When the balloon is inflated, one recognizes that each detail in the image is laterally expanded in accordance with a uniform shape transformation. In addition, the interference order $2Dn_o/\lambda$ in each spot decreases continuously as a consequence of the decreasing film thickness. Qualitatively, the same is observed for balloons in the isotropic and Sm-*A* phases. The balloon radius in Fig. 11 changes in total by a factor of 1.19. Consequently, the local value of $2Dn_o/\lambda$, (initially near 5.0) is expected to decrease to ≈3.6. In the images, one recognizes that each individual spot passes one interference maximum (4.0) and two minima (4.5 and 3.5). This result is of course only semiquantitative since the orientation of the optic axis as well as the effective refractive indices may change if the balloon deformation couples to mesogen orientations. Moreover, only a superposition of the images of rear and front sides of the balloon is

observed. However, it is obvious that the changes in interference order, and consequently the film thickness changes, are in the correct order of magnitude as expected from the presumed incompressibility of the LCE.

V. CONCLUSIONS AND SUMMARY

It has been shown that the smectic mesophases of the precursor polymers are preserved in the cross-linked materials. In the free-standing film geometry, the smectic layer orientation is parallel to the local film plane. This is confirmed by reflection microscopy images that show the formation of smectic layer steps during the isotropic Sm-*A* transition of the polymer films. From x-ray data of samples cross linked in the Sm-*A* phase, the layer structure can be quantitatively studied. We find a characteristic increase of the layer spacing with temperature in the Sm-*C** phase, which can be attributed to a temperature driven tilt angle variation of the mesogens, with a tilt angle of $\approx 20°$ in Inter3/05 far from the Sm-*A*–Sm-*C** transition. In the Sm-*A* phase, the layer thickness decreases with increasing temperature. A temperature dependent order parameter variation is not sufficient to explain this behavior. Rather, the most likely explanation is a structural change, e.g., an interpenetration of adjacent layers. At the clearing point, the SAXD reflex due to layering disappears, i.e., there is no bulk smectic order in the isotropic phase of the elastomer. However, layer steps at the film surface persist and are still observed in reflection microscopy images.

For studies of the elastic LCE behavior, bubbles have been cross linked in the Sm-*A* phase. The elasticity of the balloons in the isotropic phase as well as in the Sm-*A* phase is well described within the Mooney-Rivlin model. Elastic coefficients determined in both the phases differ only by a few percent, and hence the stress-strain characteristics are qualitatively similar. The results indicate that smectic layer compression does not measurably contribute to the stress-strain characteristics, presumably because the smectic modulus B is small compared to the entropy-related elastic moduli. If this interpretation is correct, its magnitude is considerably lower than that estimated from de Gennes' relation $B = K/d^2$ [48] (with a smectic layer thickness $d \approx 5$ nm and an elastic constant $K \approx 10^{-11}$ N). If we assume that the materials studied here possess a stratified substructure, divided into a mesogen layer and a siloxane backbone layer, as reported for similar materials [38], it is conceivable that film compression effects mainly the siloxane. Then, the modulus of the investigated LCE samples might be much lower than that of homopolymer or conventional monomer smectics.

Interestingly, the stress-strain characteristics differ qualitatively in the tilted Sm-*C** phase of interlayer and intralayer elastomers. While the Sm-*C** data are compatible with the Mooney-Rivlin model in the intralayer material Intra2/25, significant deviations have been observed for the interlayer material Inter3/05 that cannot be reconciled with that model. An explanation lies obviously in the distinct ways of coupling of mesogenic and cross-linker units in the two types of materials. If the sample is stretched within the plane, the mesogenic groups may tilt and the cross-linker groups can thus increase the lateral strain without entropy changes of the polymer chain. A similar effect has been discussed for nematic elastomers [5], and the term ''soft elasticity'' has been coined for a behavior that leads to a plateau in the stress versus strain curves. In the Sm-*C** phase of Inter3/05, such an effect is indeed indicated by the deviations of the experimental data from the entropy-elasticity model that is set in above a certain strain threshold [$R/R_0 \approx 1.05$, see Fig. 8(b)]. In the Sm-*A* phase, such a coupling could be well conceivable. However, the threshold might be much higher since the mesogens are initially perpendicular to the stretching direction. A slight deviation from the Mooney-Rivlin curve at high strain [see Fig. 8(c)] might be indicative of such a scenario, but is barely outside the level of experimental uncertainty.

Future experiments will be directed toward optical investigations of planar films to determine the interdependence of mesogenic and network mechanics. Planar films are advantageous for optical studies. However, the preparation of submicrometer planar films with two opposite supports and free lateral edges for mechanical deformations is much more difficult than the experiments in balloon geometry. Experimental efforts are also directed to the study of homopolymers where much larger contributions of the smectic layer compression modulus are expected.

ACKNOWLEDGMENTS

The authors are particularly indebted to Dr. J.-J. Li for valuable comments and discussions. We acknowledge technical assistance by Th. John and J. Pittler and encouraging discussions with F. Kremer. This study was supported by the DFG within Sonderforschungsbereich 294, TP F4, G10. M. L. acknowledges generous support by the Fond der Chemischen Industrie, Frankfurt.

[1] W. Gleim and H. Finkelmann, in *Side Chain Liquid Crystalline Polymers*, edited by C. B. McArdle (Blackie, Glasgow, 1989); H. Finkelmann, in *Liquid Crystallinity in Polymers*, edited by A. Ciferri (VCH, Weinheim, 1991).
[2] R. Zentel, Angew. Chem. **101**, 1437 (1989).
[3] F. J. J. Davis, Mater. Chem. **3**, 551 (1993).
[4] S. M. Kelly, Liq. Cryst. **24**, 71 (1998).
[5] E. M. Terentjev, J. Phys.: Condens. Matter **11**, R239 (1999).
[6] G. C. L. Wong, W. H. De Jeu, H. Shao, K. S. Liang, and R. Zentel, Nature (London) **389**, 576 (1997).
[7] P. de Gennes, M. Hébert, and R. Kant, Macromol. Symp. **113**, 39 (1997).
[8] H. Wermter and H. Finkelmann, e-Polymers 2001, No. 13, http://www.e-polymers.org
[9] T. Eckert and H. Finkelmann, Macromol. Rapid Commun. **17**, 767 (1996).
[10] K. Semmler and H. Finkelmann, Macromol. Chem. Phys. **196**, 3197 (1995).

[11] H. Finkelmann, E. Nisikawa, G. G. Pereira, and M. Warner, Phys. Rev. Lett. **87**, 015501 (2001).
[12] S. M. Clarke, A. R. Tajbakhsh, E. M. Terentjev, and M. Warner, Phys. Rev. Lett. **86**, 4044 (2001).
[13] Y. Mao and M. Warner, Phys. Rev. Lett. **86**, 5309 (2001).
[14] M. Warner, E. M. Terentjev, R. B. Meyer, and Y. Mao, Phys. Rev. Lett. **85**, 2320 (2000).
[15] B. Taheri, A. F. Muñoz, P. Palffy-Muhoray, and R. Twieg, Mol. Cryst. Liq. Cryst. Sci. Technol., Sect. A **358**, 73 (2001).
[16] H. Finkelmann, S. T. Kim, A. Muñoz, P. Palffy-Muhoray, and B. Taheri, Adv. Mater. **13**, 1069 (2001).
[17] M. Brehmer *et al.*, Macromol. Chem. Phys. **195**, 1891 (1994).
[18] M. Brehmer and R. Zentel, Macromol. Rapid Commun. **16**, 659 (1995).
[19] I. Benné, K. Semmler, and H. Finkelmann, Macromolecules **28**, 1854 (1995).
[20] M. Brehmer *et al.*, Liq. Cryst. **21**, 589 (1996).
[21] E. Gebhard and R. Zentel, Macromol. Chem. Phys. **201**, 911 (2000).
[22] S. U. Valerien *et al.*, Macromolecules **11**, 593 (1990).
[23] W. Lehmann, H. Skupin, C. Tolksdorf, E. Gebhard, R. Zentel, P. Krüger, M. Lösche, and F. Kremer, Nature (London) **410**, 447 (2001).
[24] E. Gebhard and R. Zentel, Liq. Cryst. **26**, 299 (1999).
[25] S. V. Shilov *et al.*, Liq. Cryst. **22**, 203 (1997).
[26] H. Skupin *et al.*, J. Macromol. Sci., Phys. **B38**, 709 (1999).
[27] H. M. Brodowsky *et al.*, Langmuir **15**, 274 (1999).
[28] W. Lehmann *et al.*, Ferroelectrics **208-209**, 373 (1998).
[29] W. Lehmann *et al.*, Ferroelectrics **243**, 107 (2000).
[30] H. Hirschmann, D. Velasco, H. Reinecke, and H. Finkelmann, J. Phys. II **1**, 559 (1991).
[31] I. Kundler, E. Nishikawa, and H. Finkelmann, Macromol. Symp. **117**, 11 (1997); E. Nishikawa, H. Finkelmann, and H. R. Brand, Macromol. Rapid Commun. **18**, 65 (1997).
[32] H. Schüring, R. Stannarius, C. Tolksdorf, and R. Zentel, Macromolecules **34**, 3962 (2001).
[33] H. Schüring, R. Stannarius, C. Tolksdorf, and R. Zentel, Mol. Cryst. Liq. Cryst. Sci. Technol., Sect. A **364**, 305 (2001).
[34] R. Köhler *et al.* (unpublished).
[35] C. Ortiz, C. K. Ober, and E. J. Kramer, Polymer **39**, 3713 (1998).
[36] P. M. S. Roberts, G. R. Mitchell, and F. J. Davis, J. Phys. II **7**, 1337 (1997); P. M. S. Roberts, G. R. Mitchell, F. J. Davis, and J. A. Pople, Mol. Cryst. Liq. Cryst. Sci. Technol., Sect. A **299**, 181 (1997).
[37] F. Schmidt, J. Siepmann, W. Stille, and G. R. Strobl, Mol. Cryst. Liq. Cryst. Sci. Technol., Sect. A **350**, 103 (2000).
[38] S. Diele *et al.*, Macromol. Chem. Phys. **188**, 1993 (1987).
[39] R. Stannarius and Ch. Cramer, Europhys. Lett. **42**, 43 (1998).
[40] The term ''bubble'' will be used here to describe the in-layer liquid structures (of the native polymer), while the term ''balloon'' describes the cross-linked elastomer films.
[41] P. Krüger, M. Schalke, J. Linderholm, and M. Lösche, Rev. Sci. Instrum. **72**, 184 (2001).
[42] R. Stannarius, C. Cramer, and H. Schüring, Mol. Cryst. Liq. Cryst. Sci. Technol., Sect. A **329**, 1035 (1999); **350**, 297 (2000).
[43] Supporting information in Ref. [32].
[44] See, e.g., *Polymere Werkstoffe*, edited by H. Batzer (Thieme, Stuttgart, 1985), Vol. 1.
[45] R. Köhler, Diplomarbeit, Leipzig, 2001.
[46] N. W. Tschoegl, *The Phenomenological Theory of Linear Elastic Behavior* (Springer, Heidelberg, 1989).
[47] In the notation of Ref. [5], the relation reads $p=[\mu_0+\mu_1/2](4D_0/R_0)\varepsilon$.
[48] P. G. de Gennes, *The Physics of Liquid Crystals* (Oxford University Press, New York, 1974), p. 296ff.